


Julian Ungerer^{1,*}
Ann-Kathrin Thurm²
Georg Garnweitner²
Hermann Nirschl¹

Formation of Aluminum-Doped Zinc Oxide Nanocrystals via the Benzylamine Route at Low Reaction Kinetics

The influence of essential process parameters on the adjustability of specific process and particulate properties of aluminum-doped zinc oxide (AZO) nanocrystals during synthesis via the benzylamine route at low reaction kinetics is demonstrated by enabling time-resolved access of the selected measurement technique. It is shown that the validity of the pseudo-first-order process kinetics could be extended to the minimum operable reaction kinetics. On the other hand, the impacts of the process temperature and the initial precursor concentration on both the process kinetics and the particle morphology are discussed. The obtained data provide a versatile tool for precise process control by adjusting defined application-specific particle properties of AZO during synthesis.

 This is an open access article under the terms of the Creative Commons Attribution License, which permits use, distribution and reproduction in any medium, provided the original work is properly cited.

Keywords: Aluminum-doped zinc oxide, Low reaction kinetics, Particle morphology, Pseudo-first-order kinetics, Time-resolved analysis

Received: August 27, 2019; *accepted:* February 6, 2020

DOI: 10.1002/ceat.201900466

1 Introduction

The *n*-type semiconductor, aluminum-doped zinc oxide (AZO), offers versatile applications due to its special properties, e.g. low electrical resistance, good mechanical stability, and high degree of transparency in the visible range. Due to these properties, AZO is considered to be a significantly cheaper and non-toxic alternative in order to replace, in the future, existing and finite indium-based oxides in diverse applications, such as thin-film solar modules, touch panels, light-emitting diodes, or printable electronics. Especially the application of AZO as transparent conducting oxide (TCO) in thin-film solar modules has high potential with regard to sustainable energy generation from renewable sources [1–5]. Therefore, the availability of high-quality nanocrystals with fitted sizes and shapes of crystals is required [2, 4]. In contrast to gas-phase and solid-phase processes [6] or co-precipitation [7], solvent-based liquid-phase syntheses result in better process control with moderate reaction rates [8, 9]. This synthesis route provides time-resolved access to measurement technologies in terms of particle formation analysis, as will be shown in this work. For synthesizing highly crystalline metal oxide nanostructures, the non-aqueous sol-gel synthesis is used, wherein crystalline precursors are dissolved in aromatic solvents and converted to nanoscale crystals with defined sizes, narrow particle size distributions, and adjustable morphologies, at moderate temperatures [10–14]. The work by Zellmer et al. [14] has shown time-resolved studies of crystal growth of AZO nanocrystals via the benzylamine route, preferably at high temperatures ($\sim 200^\circ\text{C}$), high precursor concentrations ($\sim 50\text{ g L}^{-1}$), and relatively short reaction times ($\sim 30\text{ min}$). However, in order to be able to

resolve the crystal growth more accurately using a measurement technique, longer reaction rates at lower process temperatures are desirable. In our previous paper, the growth behavior of AZO nanocrystals via the benzylamine route at low process temperatures ($\sim 110^\circ\text{C}$) was already successfully investigated by using small-angle X-ray scattering (SAXS) [15]. Following on from this, in our current work, the process parameters are to be extended to lower process temperatures ($T_R \leq 120^\circ\text{C}$) and initial precursor concentrations ($C_E \leq 25\text{ g L}^{-1}$), and their influences on the crystal growth kinetics and the particle morphology are to be investigated.¹⁾ In detail, we will clarify in a first step whether the already proven pseudo-first-order reaction kinetics of AZO nanocrystal synthesis via the benzylamine route at constant $T_R = 110^\circ\text{C}$ from our previous work will also be valid by extending to lower process temperatures in the range of $80^\circ\text{C} \leq T_R \leq 120^\circ\text{C}$. Quantitative phase analysis (QPA) by X-ray scattering and gravimetric analysis will be used

¹⁾Julian Ungerer, Dr. Hermann Nirschl
julian.ungerer@kit.edu

Institute for Mechanical Process Engineering and Mechanics, Karlsruhe Institute of Technology (KIT), Kaiserstrasse 12, 76131 Karlsruhe, Germany.

²⁾Ann-Kathrin Thurm, Prof. Georg Garnweitner

Institute for Particle Technology and Laboratory for Emerging Nanometrology, Technische Universität Braunschweig, Volkmaroder Strasse 5, 38104 Braunschweig, Germany.

1) List of symbols at the end of the paper.

to describe the ongoing consumption and growth processes, independent of the particle morphology and the aggregation state. Furthermore, the impact of significant process parameters (T_R , C_E) on the growth kinetics of AZO nanocrystals will be investigated in more detail using the Arrhenius model. Finally, transmission electron microscopy (TEM) and dynamic light scattering (DLS) will be used to explore the question of how much the particle properties (e.g., size, shape, crystallinity, etc.) can be influenced by the process parameters discussed above.

2 Material and Methods

2.1 Synthesis of AZO via the Benzylamine Route

For the non-aqueous sol-gel synthesis of AZO nanocrystals via the benzylamine route, the crystalline precursors zinc acetylacetonate hydrate ($\text{Zn}(\text{acac})_2$ powder, $\geq 99\%$; Aldrich) and aluminum isopropoxide ($\text{Al}(\text{OiPr})_3$, $\geq 98\%$; Aldrich) in the initial concentration range of $6.25 \text{ g L}^{-1} \leq C_E \leq 25 \text{ g L}^{-1}$ were used, wherein the molar fraction of the aluminum precursor was set to 2.5 mol%. The aromatic solvent benzylamine (BnNH_2 , benzylamine for synthesis, $\geq 99\%$; Merck) served as reaction medium. For a detailed description of the synthesis and sampling procedure at low process temperatures in the range of $80^\circ\text{C} \leq T_R \leq 120^\circ\text{C}$ using a closed and ideally stirred batch reactor, we refer to our previous work [15]. Due to the physical limitation with regard to the $\text{Zn}(\text{acac})_2$ solubility at $T_R \ll 50^\circ\text{C}$, the minimum solution-limited process temperature for the reaction system used was set at $T_R = 80^\circ\text{C}$.

2.2 Sample Purification and Characterization Methods

For the time-resolved access of measurement techniques to the synthesis for analyzing the AZO nanocrystal growth behavior, we developed a new sample purification procedure considering both the solubility limit of $\text{Zn}(\text{acac})_2$ and the high corrosivity of BnNH_2 with regard to the measurement techniques used. The sequence of the individual sample preparation steps, including their associated analysis methods, is shown in Fig. 1.

During the synthesis at $T_R \geq 80^\circ\text{C}$, only AZO is present as crystalline phase in the solvent BnNH_2 . After sampling and rapid cooling at different reaction times $t < t_{\text{END}}$, the unreacted

precursor $\text{Zn}(\text{acac})_2$ precipitated completely at $T_R \approx 25^\circ\text{C}$ due to its poor solubility in BnNH_2 , and thus the two crystalline phases $\text{AZO}/\text{Zn}(\text{acac})_2$ were present in BnNH_2 . Applying QPA analysis using our self-developed SAXS laboratory camera (for more details on the analytical procedure, see [15–17]), it was possible to quantify the time-resolved consumption concentration $C_{\text{Zn}(\text{acac})_2}$ (g L^{-1}) of crystalline $\text{Zn}(\text{acac})_2$ based on the scattering intensity $I_{2\theta=16^\circ}^{\text{Zn}(\text{acac})_2}$ at constant scattering angle $2\theta = 16^\circ$, as shown in Eq. (1).

$$C_{\text{Zn}(\text{acac})_2} = (259 \pm 7\%) I_{2\theta=16^\circ}^{\text{Zn}(\text{acac})_2} \quad (1)$$

In the subsequent washing process, two purification steps were carried out: In the first step, BnNH_2 was removed by centrifugation for 15 min with a force of $7200 \times g$ at 20°C (centrifuge 5430R; Eppendorf). In the second step, the ethanol-soluble $\text{Zn}(\text{acac})_2$ crystals were completely separated from AZO by washing twice with ethanol, in excess by factor 4, by re-centrifugation. To characterize the particle properties of AZO at the end of their growth, the AZO particles present in pure ethanol were then analyzed by DLS, using a Zetasizer (Nano ZS; Malvern), and by TEM (Osiris ChemiStem; FEI). For TEM, the samples had to be diluted with ethanol and air-dried on a TEM grid at 25°C . Finally, for recording the AZO concentration C_{AZO} (g L^{-1}) by gravimetric analysis, the nanocrystals were completely dried at 80°C for 24 h under ambient pressure in a drying oven (UN260; Memmert) and afterwards quantified with an analytical scale (Secura 224-1S; Sartorius) by using Eq. (2), depending on the sampling volume V_s and the dry matter m_{AZO} .

$$C_{\text{AZO}} = \frac{m_{\text{AZO}}}{V_s} \quad (2)$$

2.3 Kinetic Model Describing the AZO Nanocrystal Synthesis

For a quantitative description of the consumption and growth processes during the AZO synthesis via the benzylamine route, the pseudo-first-order kinetics model was used. For the purpose of applying this model to the AZO synthesis, several assumptions, which are described in more detail in ref. [15], were made for simplicity, in order to get the final expression of the product formation rate r_{AZO} in Eq. (3), depending on the

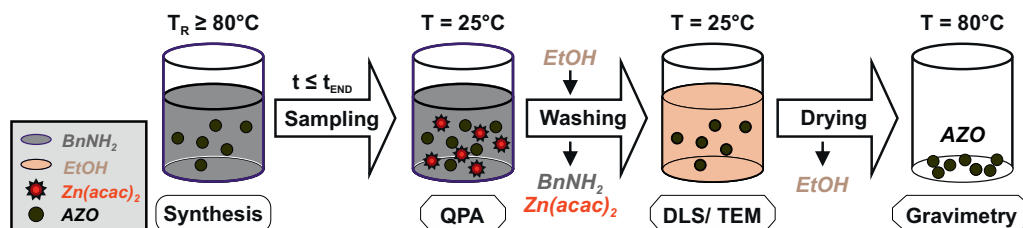


Figure 1. Sequence of the newly developed sample purification steps after sampling and the associated analysis methods for time-resolved characterization of the AZO nanocrystal synthesis via the benzylamine route.

unreacted zinc precursor concentration $C_{\text{Zn}(\text{acac})_2}(t)$ and the rate constant k (s^{-1}).

$$r_{\text{AZO}}(t) = -\frac{dC_{\text{Zn}(\text{acac})_2}}{dt} = kC_{\text{Zn}(\text{acac})_2}(t) \quad (3)$$

After separation of the variables, integration, and exponentiation, a pseudo-first-order model resulted in Eq. (4), describing a time-dependent exponential consumption of $C_{\text{Zn}(\text{acac})_2}(t)$ as a function of the initial zinc precursor concentration $C_{\text{Zn}(\text{acac})_2}(0)$.

$$C_{\text{Zn}(\text{acac})_2}(t) = C_{\text{Zn}(\text{acac})_2}(0)e^{-kt} \quad (4)$$

In the case of full conversion, the pseudo-first-order model of restricted exponential growth of the AZO concentration $C_{\text{AZO}}(t)$ resulted in Eq. (5) with an equal rate constant.

$$C_{\text{AZO}}(t) = C_{\text{AZO}}(\infty)(1 - e^{-kt}) \quad (5)$$

3 Results and Discussion

3.1 Validity of the Pseudo-First-Order Kinetics in the Low Process Temperature Range

In this section, the validity of the pseudo-first-order kinetics, which was already successfully demonstrated in our previous work for $T_{\text{R}} = 110^\circ\text{C}$, is to be demonstrated at the minimum operable process temperature, $T_{\text{R}} = 80^\circ\text{C}$, and thus for the low temperature range, $80^\circ\text{C} \leq T_{\text{R}} \leq 120^\circ\text{C}$, investigated in this work [15]. For a better comparability of both kinetics, the normalized pseudo-first-order growth model function of AZO from Eq. (5), based on gravimetric data, and the normalized pseudo-first-order consumption model function of $\text{Zn}(\text{acac})_2$ from Eq. (4), based on QPA by SAXS data using Eq. (1), from our previous work at $T_{\text{R}} = 110^\circ\text{C}$ (dashed lines, $\bar{R}^2 > 99\%$) are plotted next to the here observed equivalent growth and consumption kinetics at $T_{\text{R}} = 80^\circ\text{C}$ (solid lines, $\bar{R}^2 > 98\%$) in Fig. 2.

In Fig. 2, the qualitative trajectories of the respective growth and consumption functions form an intersection at a concentration ratio of approximately 50%. This fact suggests a similar kinetics of the consumption and growth process at both process temperatures, indicating the validity of the pseudo-first-order kinetics even at $T_{\text{R}} = 80^\circ\text{C}$. The final proof can be provided by the comparison of each consumption ($k_{\text{Zn}(\text{acac})_2}$) and growth (k_{AZO}) rate constant, calculating their relative deviation $\Delta k_{\text{AZO}/\text{Zn}(\text{acac})_2}$ as listed in Tab. 1.

Taking into account the respective errors in Tab. 1, the equality of both the consumption kinetics of $\text{Zn}(\text{acac})_2$ and the growth kinetics of AZO is proven at the two investigated process conditions. This fact provides the decisive indication that the synthesis of AZO via the benzylamine route not only follows pseudo-first-order kinetics at $T_{\text{R}} = 110^\circ\text{C}$, as shown in our previous work, but also at the minimum $T_{\text{R}} = 80^\circ\text{C}$. Thus, the validity of the reaction order can be extended to the entire low process temperature range of $80^\circ\text{C} \leq T_{\text{R}} \leq 120^\circ\text{C}$ investigated in this work.

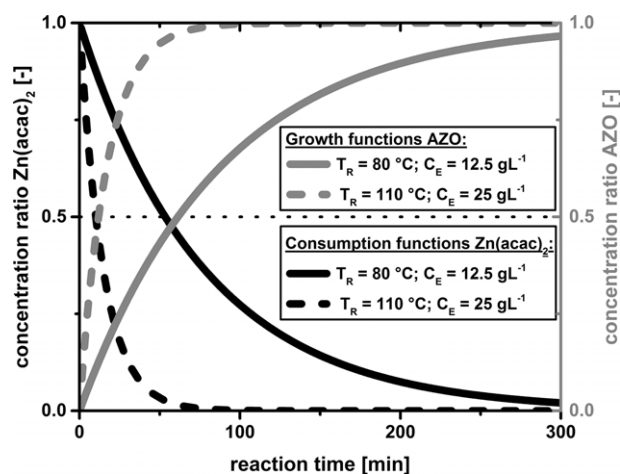


Figure 2. Normalized pseudo-first-order $\text{Zn}(\text{acac})_2$ consumption model functions based on QPA data by SAXS and associated normalized pseudo-first-order AZO growth model functions from gravimetric data at two different process conditions: $T_{\text{R}} = 80^\circ\text{C}$, $C_{\text{E}} = 12.5 \text{ g L}^{-1}$ (synthesis 1, solid lines) and $T_{\text{R}} = 110^\circ\text{C}$, $C_{\text{E}} = 25 \text{ g L}^{-1}$ (synthesis 2 from previous work [15], dashed lines).

Table 1. Consumption and growth rate constants $k_{\text{Zn}(\text{acac})_2}$, k_{AZO} , the relative mean deviation of both rate constants $\Delta k_{\text{AZO}/\text{Zn}(\text{acac})_2}$, and the mean coefficients of determination at two different process conditions, $T_{\text{R}} = 80^\circ\text{C}$, $C_{\text{E}} = 12.5 \text{ g L}^{-1}$ (synthesis 1) and $T_{\text{R}} = 110^\circ\text{C}$, $C_{\text{E}} = 25 \text{ g L}^{-1}$ (synthesis 2 from previous work [15]).

Process parameter	Synthesis 1	Synthesis 2
	$T_{\text{R}} = 80^\circ\text{C}$, $C_{\text{E}} = 12.5 \text{ g L}^{-1}$	$T_{\text{R}} = 110^\circ\text{C}$, $C_{\text{E}} = 25 \text{ g L}^{-1}$
$k_{\text{Zn}(\text{acac})_2} [\text{s}^{-1}]$	$2.1 \times 10^{-4} \pm 15\%$	$11.3 \times 10^{-4} \pm 15\%$
$k_{\text{AZO}} [\text{s}^{-1}]$	$1.9 \times 10^{-4} \pm 11\%$	$9.8 \times 10^{-4} \pm 8\%$
$\Delta k_{\text{AZO}/\text{Zn}(\text{acac})_2} [\%]$	10	13
$\bar{R}^2 [\%]$	98	99

3.2 Behavior of the Reaction Kinetics in the Low Process Temperature Range

In addition to the successful validation of the reaction kinetics following the pseudo-first order, even at the minimum solution-limited process temperature, Fig. 2 shows a clear shift of the intersection point along the x-axis, indicating an extension in overall process time (t_{END}) by reducing the process temperature. Since a temperature reduction of only 27% resulted in a significant extension of t_{END} by a factor of about 5, from originally $t_{\text{END}} = 56 \text{ min}$ to 285 min, this section will focus in more detail on the influence of the temperature on the reaction kinetics of the AZO synthesis. Due to the validity of the pseudo-first-order kinetics, further kinetic studies were continued only by gravimetric analysis of AZO, by investigating further process conditions in the ranges of $80^\circ\text{C} \leq T_{\text{R}} \leq 120^\circ\text{C}$ and

$6.25 \text{ g L}^{-1} \leq C_E \leq 25 \text{ g L}^{-1}$ in more detail. In Fig. 3, the normalized pseudo-first-order growth kinetic functions of AZO in the range of $80^\circ\text{C} \leq T_R \leq 120^\circ\text{C}$ based on gravimetric data ($\bar{R}^2 > 98\%$) were averaged over the entire initial precursor concentration range of $6.25 \text{ g L}^{-1} \leq C_E \leq 25 \text{ g L}^{-1}$ and finally plotted over the logarithmic reaction time.

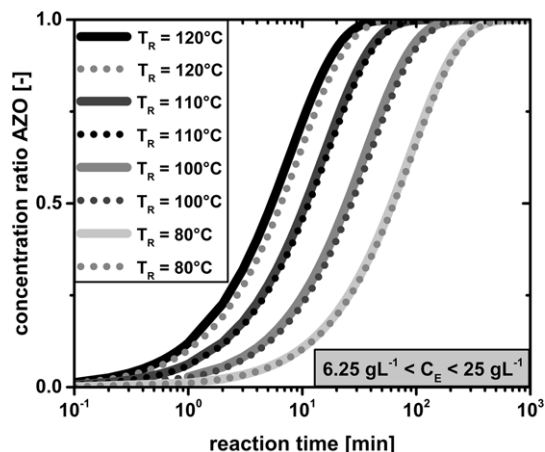


Figure 3. Temperature dependence of the normalized pseudo-first-order growth kinetic functions of AZO in the range of $80^\circ\text{C} \leq T_R \leq 120^\circ\text{C}$ based on gravimetric data ($\bar{R}^2 > 98\%$), averaged over the entire initial precursor concentration range of $6.25 \text{ g L}^{-1} \leq C_E \leq 25 \text{ g L}^{-1}$.

A good reproducibility of the gravimetric analysis method could be emphasized by a high agreement of the multiply determined data in Fig. 3 (dotted lines). An increase in process temperature obviously led to a shift of the growth functions towards smaller reaction times and thus to higher mean rate constants, which are averaged over $6.25 \text{ g L}^{-1} \leq C_E \leq 25 \text{ g L}^{-1}$ and listed in detail in Tab. 2.

Analogous to t_{END} , a high sensitivity of \bar{k} to small changes in T_R can be underpinned again in Tab. 2, since even after a change in $\Delta T_R = 40 \text{ K}$, \bar{k} already changed significantly by a factor of about 18. To quantify the temperature dependency towards the kinetics of the AZO synthesis in detail, the Arrhenius model in Eq. (6) was used.

$$k(T_R) = A e^{-\frac{E_A}{RT}} \quad (6)$$

The Arrhenius model generally describes the temperature dependence of the rate constant $k(T_R)$ of a chemical reaction process as a function of a constant pre-exponential factor A , the activation energy E_A , the universal gas constant R , and the absolute temperature T . To check, on the one hand, if the temperature dependency of the AZO synthesis process corresponds

Table 2. Mean rate constants, averaged over the initial precursor concentration range of $6.25 \text{ g L}^{-1} \leq C_E \leq 25 \text{ g L}^{-1}$, dependent on the process temperature of the investigated synthesis processes.

Process temperature T_R [$^\circ\text{C}$]	80	100	110	120
Mean rate constant \bar{k} [10^{-4} s^{-1}]	$1.51 \pm 20\%$	$4.50 \pm 5\%$	$10.2 \pm 5\%$	$19.5 \pm 9\%$

to the Arrhenius model and to determine, on the other hand, all process-relevant parameters from Eq. (6), the mean rate constants from Tab. 2 were plotted in an Arrhenius plot in Fig. 4 (black squares).

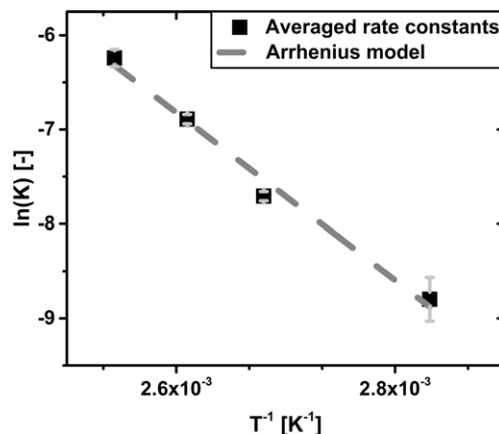


Figure 4. Logarithmic rate constants of the AZO growth model functions from Tab. 2 (black squares), averaged in terms of the initial precursor concentration range of $6.25 \text{ g L}^{-1} \leq C_E \leq 25 \text{ g L}^{-1}$ (error bars), plotted versus the reciprocal absolute process temperature in the range of $80^\circ\text{C} \leq T_R \leq 120^\circ\text{C}$ and approximated by means of linear regression of Eq. (6) with $R^2 \approx 98\%$.

By linear regression of Eq. (6) to the data in Fig. 4, the validity of the Arrhenius law could be investigated with a very high coefficient of determination ($R^2 \approx 98\%$) within the investigated process temperature range of $80^\circ\text{C} \leq T_R \leq 120^\circ\text{C}$. The parameters obtained from linear regression, such as $A = 1.16 \times 10^7 \text{ s}^{-1}$ ($\pm < 1\%$) and $E_A = 73.8 \text{ kJ mol}^{-1}$ ($\pm < 8\%$), are within the expected range for generally activation-controlled reactions [18, 19]. The negligible systematic errors in Fig. 4 and Tab. 2 underpinned the independence of the process kinetics in terms of the initial precursor concentrations under the investigated process conditions. Similar findings of strong dependence on the temperature but low influence of the precursor concentration on the reaction kinetics have also been observed for the non-aqueous formation of ZrO_2 nanoparticles in benzyl alcohol [20]. The successful description of the AZO synthesis using the Arrhenius model showed, on the one hand, the reproducibility and applicability of the measuring methods used over an extended process control range. On the other hand, the determined Arrhenius parameters represent a general tool for predicting the process kinetics of the investigated AZO synthesis via the benzylamine route, especially for higher-order kinetics at $T_R \gg 120^\circ\text{C}$, which are difficult to access with measurement techniques.

3.3 Impact on the Particle Morphology and Size

In this section, the main influencing parameters on the final particle morphology of the AZO nanocrystals at the end of their growth are to be

investigated more closely using TEM and DLS, in order to elucidate important questions about the specific influence on particle properties such as size, shape, and crystallinity. Considering a single AZO particle in Fig. 5 using TEM, synthesized at $T_R = 120\text{ }^\circ\text{C}$ and $C_E = 25\text{ g L}^{-1}$, a very high similarity to the mesocrystalline structure of AZO from our previous work can be observed, based on the typical hexagonal form and the remaining internal grain boundaries [15]. Compared to the TEM images of our earlier work, the crystalline structure parameters are more recognizable at the atomic level due to the higher resolution of the transmission electron microscope used here.

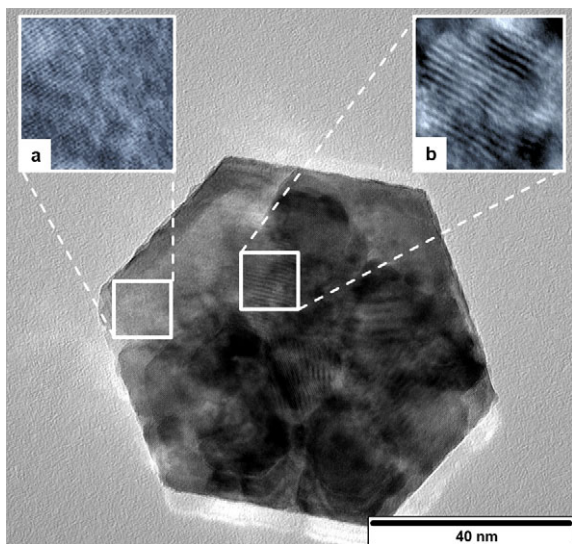


Figure 5. TEM image of a single hexagonal AZO mesocrystal after completion of growth with monocrystalline (inlet a) and polycrystalline (inlet b) regions at $T_R = 120\text{ }^\circ\text{C}$ and $C_E = 25\text{ g L}^{-1}$.

With a crystal size of $\sim 85\text{ nm}$, various crystalline regions with different mutual orientations could be seen on the particle surface, finally forming a hexagon-shaped polycrystalline particle with uniform outer edge lengths. On the one hand, monocrystalline regions with uniform lattice plane orientation could be observed on the basis of visible atomic lattice distances (inlet a in Fig. 5) and, on the other hand, polycrystalline regions could be seen, in which an overlapping of several monocrystalline lattice planes occurred (inlet b in Fig. 5). Especially, the polycrystalline areas are recognizable on the so-called Moiré stripes, which arose due to the double diffraction of electrons at superimposed crystal lattice planes with similar periodicity [21]. Both the typical hexagonal particle shape and the remaining internal grain boundaries could be attributed to a prior oriented aggregation with incomplete intergrowth during the growth process, which fits very well with the findings on the non-classical growth behavior from our prior work [15].

In order to investigate the influence of T_R and C_E on the particle morphology, the above-described AZO mesocrystal is contrasted to the final growth states at three further boundary process conditions in the ranges of $80\text{ }^\circ\text{C} \leq T_R \leq 120\text{ }^\circ\text{C}$ and $6.25\text{ g L}^{-1} \leq C_E \leq 25\text{ g L}^{-1}$ in Fig. 6a–d. Under all of the process conditions studied here, mesostructured particles of AZO with crystalline phases were formed by non-classical growth, as

shown by the Moiré stripes in Fig. 6a–d (white arrows). By comparing Fig. 6a, c at $C_E = 25\text{ g L}^{-1} = \text{const.}$ and Fig. 6b, d at $C_E = 6.25\text{ g L}^{-1} = \text{const.}$, it could be shown that the crystallinity of the observed AZO mesocrystals is more pronounced with rising T_R , as evidenced by the more regular shape and the smoother outer surfaces of the single mesocrystals from Fig. 6a, b (white dashed lines). Diffuse areas at the particle surfaces at the minimum reaction kinetics in Fig. 6c, d (black arrows) indicated either amorphous structures – and thus partial crystallinity of the final AZO particles – or non-removable organic solvent residues. The increasing crystallinity at increasing T_R could be explained by the higher energy supply for applying the required lattice energy in the formation of the crystalline lattice, on the one hand, and an annealing of the agglomeration-induced crystal defects by increased diffusion during synthesis, on the other hand [22].

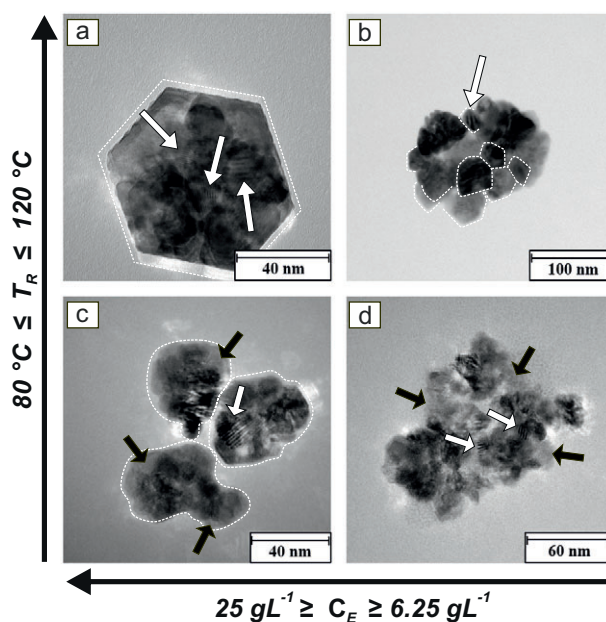


Figure 6. Comparison of the final growth states of the mesocrystalline AZO nanocrystals (white dashed lines) by TEM, at the four boundary process conditions (a–d) of the ranges $80\text{ }^\circ\text{C} \leq T_R \leq 120\text{ }^\circ\text{C}$ and $6.25\text{ g L}^{-1} \leq C_E \leq 25\text{ g L}^{-1}$.

At $T_R = 120\text{ }^\circ\text{C} = \text{const.}$, magnification of the AZO mesocrystals in Fig. 6a, b was observed after increasing C_E , which could be more accurately quantified by the increase of the mean equivalent diameter of mesocrystals from $\bar{d}_{50,0} = 61.36\text{ nm} \pm 4\%$ at $C_E = 6.25\text{ g L}^{-1}$ to $\bar{d}_{50,0} = 90.43\text{ nm} \pm 3\%$ at $C_E = 25\text{ g L}^{-1}$ using DLS. In addition, the DLS results at $T_R = 80\text{ }^\circ\text{C} = \text{const.}$ have shown a similar tendency due to the increase from $d_{50,0} = 60.87\text{ nm} \pm 2\%$ to $d_{50,0} = 86.16\text{ nm} \pm 5\%$, which obviously could not be noticed by comparing Fig. 6c, d due to the amorphous matrix. Both the mesocrystal sizes from DLS at $C_E = 6.25\text{ g L}^{-1} = \text{const.}$ and at $C_E = 25\text{ g L}^{-1} = \text{const.}$ showed similar values, respectively, independently of the process temperature, resulting in no significant influence of the process temperature on the final mesocrystal size of AZO, as also shown in the work of Zellmer et al. [14].

4 Conclusions

The major finding of this work is the demonstration of the impact of essential process parameters on the particle and process properties during non-classical growth of AZO mesocrystals via the benzylamine route in the low temperature range of $80\text{ }^{\circ}\text{C} \leq T_{\text{R}} \leq 120\text{ }^{\circ}\text{C}$ and the initial precursor concentration range of $6.25\text{ g L}^{-1} \leq C_{\text{E}} \leq 25\text{ g L}^{-1}$, by getting time-resolved access with selected measurement techniques. It could generally be observed that, on the one hand, both the growth kinetics and the crystalline properties of AZO were significantly influenced by the process temperature setting while, on the other hand, the final mesocrystal size was predominantly controlled by the initial precursor concentration. In detail, the validity of the already proven pseudo-first-order kinetics for the overall AZO nanocrystal synthesis via the benzylamine route at $T_{\text{R}} = 110\text{ }^{\circ}\text{C}$ could also be successfully demonstrated for the solution-limited minimum process temperature of $T_{\text{R}} = 80\text{ }^{\circ}\text{C}$ by QPA and gravimetric analysis, thus expanding the validity of the process kinetics throughout the low temperature range of $80\text{ }^{\circ}\text{C} \leq T_{\text{R}} \leq 120\text{ }^{\circ}\text{C}$ examined in this work. Furthermore, a very strong process temperature influence on the process kinetics was observed using gravimetric analysis, which could be successfully approximated to the Arrhenius model, agreeing with kinetics parameters of similar works and expectations of an activation-controlled synthesis. Finally, in accordance with our previous work, a non-classical mesocrystal growth of AZO could be observed in the studied parameter range by TEM and DLS, demonstrating both a visibly increasing crystallinity by raising the process temperature and an enlargement of the final AZO mesocrystals by increasing the initial precursor concentration. The detailed knowledge gained in this work on the two important process-influencing parameters, the process temperature, on the one hand, and the initial precursor concentration, on the other hand, is generally a versatile tool for precise process control by adjusting defined application-specific particle properties of AZO nanocrystals during synthesis.

Acknowledgments

The research leading to these results has received funding from the German Research Foundation (DFG Ni 414/24-1 and Ga 1492/9-1). We express our immense thanks to Mr. Tim Köhler, Mr. Florian Kaiser, and Mr. Tim Delrieux for the experimental assistance and Mrs. Sabrina Zellmer for fruitful discussions.

The authors have declared no conflict of interest.

Symbols used

A	$[\text{s}^{-1}]$	pre-exponential factor
C	$[\text{g L}^{-1}]$	mass concentration
C_{E}	$[\text{g L}^{-1}]$	initial precursor concentration
$\bar{d}_{50,0}$	$[\text{nm}]$	number-weighted mean diameter
E_{A}	$[\text{kJ mol}^{-1}]$	activation energy
I	$[\text{a.u.}]$	scattering intensity

k	$[\text{s}^{-1}]$	first-order rate constant
\bar{k}	$[\text{s}^{-1}]$	mean rate constant
m	$[\text{g}]$	dry matter
r	$[\text{kg L}^{-1}\text{s}^{-1}]$	formation rate
R	$[\text{J mol}^{-1}\text{K}^{-1}]$	universal gas constant
\bar{R}^2	$[-]$	mean coefficient of determination
t	$[\text{s}]$	reaction time
t_{END}	$[\text{s}]$	time after 97 % of reaction conversion
T_{R}	$[\text{ }^{\circ}\text{C}]$	process temperature
T	$[\text{K}]$	absolute temperature
V_{s}	$[\text{L}]$	sampling volume

Greek symbols

Δ	$[-]$	mean deviation
2θ	$[\text{ }^{\circ}]$	scattering angle

Abbreviations

AZO	aluminum-doped zinc oxide
Al(OiPr) ₃	aluminum isopropoxide
BnNH ₂	benzylamine
DLS	dynamic light scattering
EtOH	ethanol
QPA	quantitative phase analysis
SAXS	small-angle X-ray scattering
TCO	transparent conducting oxide
TEM	transmission electron microscopy
Zn(acac) ₂	zinc acetylacetonate hydrate

References

- [1] X. Jiang et al., Aluminum-doped zinc oxide films as transparent conductive electrode for organic light-emitting devices, *Appl. Phys. Lett.* **2003**, *83* (9), 1875–1877.
- [2] L. Luo et al., Microwave-assisted nonaqueous sol-gel synthesis: from Al:ZnO nanoparticles to transparent conducting films, *ACS Sustainable Chem. Eng.* **2012**, *1* (1), 152–160.
- [3] T. Minami, Transparent conducting oxide semiconductors for transparent electrodes, *Semicond. Sci. Technol.* **2005**, *20* (4), S35.
- [4] T. Strachowski et al., Morphology and luminescence properties of zinc oxide nanopowders doped with aluminum ions obtained by hydrothermal and vapor condensation methods, *J. Appl. Phys.* **2007**, *102* (7), 073513.
- [5] C. R. Ellinger, S. F. Nelson, Selective area spatial atomic layer deposition of ZnO, Al₂O₃, and aluminum-doped ZnO using poly(vinyl pyrrolidone), *Chem. Mater.* **2014**, *26* (4), 1514–1522.
- [6] M. Yoon et al., Solid solubility limits of Ga and Al in ZnO, *J. Mater. Sci. Lett.* **2002**, *21* (21), 1703–1704.
- [7] D. Nie et al., Synthesis and structure analysis of aluminum doped zinc oxide powders, *Sci. China, Ser. B: Chem.* **2008**, *51* (9), 823–828.

- [8] B. L. Cushing, V. L. Kolesnichenko, C. J. O'Connor, Recent advances in the liquid-phase syntheses of inorganic nanoparticles, *Chem. Rev.* **2004**, *104* (9), 3893–3946.
- [9] J. Livage, M. Henry, C. Sanchez, Sol-gel chemistry of transition metal oxides, *Progr. Solid State Chem.* **1988**, *18* (4), 259–341.
- [10] T. A. Cheema, G. Garnweitner, Phase-controlled synthesis of ZrO₂ nanoparticles for highly transparent dielectric thin films, *CrystEngComm* **2014**, *16* (16), 3366–3375.
- [11] P. Stolzenburg et al., Fractal growth of ZrO₂ nanoparticles induced by synthesis conditions, *CrystEngComm* **2016**, *18* (43), 8396–8405.
- [12] G. Garnweitner et al., Benzylamines as versatile agents for the one-pot synthesis and highly ordered stacking of anatase nanoplatelets, *Eur. J. Inorg. Chem.* **2008**, *2008* (6), 890–895.
- [13] G. Garnweitner, M. Niederberger, Organic chemistry in inorganic nanomaterials synthesis, *J. Mater. Chem.* **2008**, *18* (11), 1171–1182.
- [14] S. Zellmer et al., Aluminum zinc oxide nanostructures with customized size and shape by non-aqueous synthesis, *CrystEngComm* **2015**, *17* (36), 6878–6883.
- [15] J. Ungerer et al., Development of a growth model for aluminum-doped zinc oxide nanocrystal synthesis via the benzylamine route, *J. Nanopart. Res.* **2019**, *21* (5), 106.
- [16] X. Guo et al., Simultaneous SWAXS study of metallic and oxide nanostructured particles, *J. Nanopart. Res.* **2013**, *15* (4), 1559.
- [17] A. Gutsche et al., Time-resolved SAXS characterization of the shell growth of silica-coated magnetite nanocomposites, *J. Nanopart. Res.* **2014**, *16* (7), 2475.
- [18] G. Clark, L. E. Smart, *Chemical Kinetics and Mechanism*, Royal Society of Chemistry, London **2007**.
- [19] J. H. Espenson, *Chemical Kinetics and Reaction Mechanisms*, vol. 102, McGraw-Hill, New York **1995**.
- [20] P. Stolzenburg, G. Garnweitner, Experimental and numerical insights into the formation of zirconia nanoparticles: A population balance model for the nonaqueous synthesis, *React. Chem. Eng.* **2017**, *2* (3), 337–348.
- [21] D. B. Williams, C. B. Carter, *Transmission Electron Microscopy, A Textbook for Materials Science*, Springer, New York **2009**.
- [22] H. S. Kang et al., Variation of light emitting properties of ZnO thin films depending on post-annealing temperature, *Mater. Sci. Eng., B* **2003**, *102* (1–3), 313–316.